



# Suppressed lithium dendrite growth in lithium batteries using ionic liquid electrolytes: Investigation by electrochemical impedance spectroscopy, scanning electron microscopy, and *in situ* $^7\text{Li}$ nuclear magnetic resonance spectroscopy

Nina Schweikert<sup>a</sup>, Andreas Hofmann<sup>b</sup>, Michael Schulz<sup>b</sup>, Marco Scheuermann<sup>a</sup>, Steven T. Boles<sup>c</sup>, Thomas Hanemann<sup>b</sup>, Horst Hahn<sup>a,d</sup>, Sylvio Indris<sup>a,\*</sup>

<sup>a</sup> Institute of Nanotechnology, Karlsruhe Institute of Technology, P.O. Box 3640, 76021 Karlsruhe, Germany

<sup>b</sup> Institute for Applied Materials – Material Process Technology, Karlsruhe Institute of Technology, P.O. Box 3640, 76021 Karlsruhe, Germany

<sup>c</sup> Institute for Applied Materials – Materials and Biomechanics, Karlsruhe Institute of Technology, P.O. Box 3640, 76021 Karlsruhe, Germany

<sup>d</sup> KIT-TUD Joint Research Laboratory Nanomaterials, Technische Universität Darmstadt, Institute of Materials Science, Petersenstr. 32, 64287 Darmstadt, Germany

## H I G H L I G H T S

- Non-invasive and quantitative investigation of Li dendrite formation in Li batteries by  $^7\text{Li}$  NMR and impedance spectroscopy.
- SEM images show good agreement with NMR and impedance results.
- The growth of lithium dendrites is significantly correlated to the electrolyte employed.
- Li dendrite growth can be suppressed by electrolytes containing ionic liquids.

## A R T I C L E I N F O

### Article history:

Received 18 July 2012

Received in revised form

27 September 2012

Accepted 16 November 2012

Available online 5 December 2012

### Keywords:

Lithium titanate

Lithium metal

Dendrite formation

Nuclear magnetic resonance

Electrochemical impedance spectroscopy

Scanning electron microscopy

## A B S T R A C T

In this work, the formation of lithium dendrites in lithium/ $\text{Li}_4\text{Ti}_5\text{O}_{12}$  battery cells is studied using different experimental techniques. Electrochemical impedance spectroscopy is presented as a tool to investigate non-invasively the dendritic growth on a lithium metal surface in lithium/ $\text{Li}_4\text{Ti}_5\text{O}_{12}$  cells during numerous discharging/charging cycles. Scanning electron microscopy is used for visual inspection of the dendrite formation. *In situ*  $^7\text{Li}$  nuclear magnetic resonance spectroscopy is sensitive to quantitative changes at the lithium metal surface. Application to symmetrical lithium/lithium battery cells allows for a careful comparison of the investigated electrolytes. All these experimental methods provide consistent results. It is demonstrated that the growth of lithium dendrites is significantly correlated to the electrolyte employed. All electrolytes based on the ionic liquid 1-ethyl-3-methylimidazolium bis(trifluoromethane-sulfonyl)azanide (EMIM-TFSA) show reduced dendrite growth in comparison to the standard electrolyte for Li-ion batteries, lithium hexafluorophosphate ( $\text{LiPF}_6$ ) in ethylene carbonate/dimethyl carbonate (EC/DMC).  $\text{LiPF}_6$  in EMIM-TFSA and  $\text{LiPF}_6$  in EMIM-TFSA/propylene carbonate suppress lithium dendrites most efficiently.

© 2012 Elsevier B.V. All rights reserved.

## 1. Introduction

Starting with its commercialization in 1991, the interest in lithium-ion batteries has strongly increased due to its application in consumer devices and, more recently, in electric vehicles. However, long before lithium-ion batteries were employed, lithium metal received much attention as anode material [1].

Due to its remarkable electrochemical characteristics, lithium metal is capable of both enhancing the capacity and reducing the weight of lithium-ion batteries [1,2]. Therefore, lithium metal electrodes are promising candidates for the next generation of batteries including, e.g., lithium/air [3–6] or lithium/sulfur systems [3,7–9]. Despite its attractive properties, the application of lithium electrodes is currently limited by the formation of the solid electrolyte interphase (SEI) [10] and dendritic growth during lithium deposition on the metal surface [2,11]. This dendrite growth results in irreversible capacity losses and safety issues [12,13]. As a requirement for successful application in commercial battery

\* Corresponding author. Tel.: +49 721 608 28312; fax: +49 721 608 26368.

E-mail address: [sylvio.indris@kit.edu](mailto:sylvio.indris@kit.edu) (S. Indris).

systems, the morphological evolution occurring at the lithium surface during cycling has to be understood.

In recent years, many imaging studies have been performed on the morphology of lithium metal including optical microscopy and scanning electron microscopy (SEM) [12,14–20]. The influence of the electrolyte and additives [15,21–24] as well as stack pressure [25] on the formation of the passivation layer has been studied. More recently, the effect of current density [19,20,26] and the total charge [26,27] have been investigated. A mathematical description of dendrite growth was reported by Yamaki *et al.* [14] and by Brissot *et al.* [28].

Ionic liquids (IL) have attracted remarkable interest for lithium-ion batteries based on their beneficial properties such as non-volatility, non-flammability, a wide electrochemical stability window, and a reasonable conductivity [29]. Furthermore, it has been shown that dendritic growth of lithium on a bare lithium surface is hindered if ionic liquids are used as electrolyte components [30]. Thus, ionic liquids exhibit a promising potential in combination with lithium metal as anode material.

In this work, we studied the properties of selected electrolytes predominantly based on ionic liquids in lithium/Li<sub>4</sub>Ti<sub>5</sub>O<sub>12</sub> battery cells during cycling with different techniques including electrochemical impedance spectroscopy (EIS) [31] and SEM. With its very flat discharge/charge plateau at 1.55 V and its excellent cycle-life [32,33], lithium/Li<sub>4</sub>Ti<sub>5</sub>O<sub>12</sub> test cells offer the possibility to gain a better understanding of the interfacial chemistry at both the working and the counter electrodes [34,35]. *In situ* <sup>7</sup>Li nuclear magnetic resonance (NMR) [36] was applied to symmetrical lithium/lithium battery cells during the initial half-cycle. This experimental setup permits the acquisition of unbiased NMR spectra in order to compare the different electrolytes.

## 2. Experimental

### 2.1. Reagents

1-Ethyl-3-methylimidazolium bis(trifluoromethanesulfonyl)azanide<sup>1</sup>(EMIM-TFSA, Iolitec), lithium bis(trifluoromethanesulfonyl)azanide (LiTFSA, Iolitec), ethylene carbonate (EC, Sigma–Aldrich, anhydrous, 99%), and propylene carbonate (PC, Sigma–Aldrich, anhydrous, 99.7%) were dried at 110 °C by means of a continuous flow of dried air. The water content of the solvents was determined by Karl Fischer titration to be less than 10 ppm. Lithium hexafluorophosphate (LiPF<sub>6</sub>, ABCR, battery grade, 99.9%) and LP-30 (Merck, EC/DMC 1:1-w, 1 M LiPF<sub>6</sub>) were used as received. The preparation of the electrolytes was performed in an argon-filled glove box (MBraun GmbH) with oxygen and water levels smaller than 0.5 ppm. The composition and selected conductivity and viscosity data of the electrolytes are listed in Table 1.

### 2.2. Ionic conductivity and viscosity measurements

For the conductivity measurements, a Swagelok-type cell design was used by placing a Teflon spacer between two stainless steel cylinders (diameter 12.7 mm). Via a small hole in the Teflon ring, the electrolyte was filled in. The cell assembly was done under protective atmosphere. The ionic conductivity is calculated from  $\sigma = L/(A \cdot R_b)$ , where  $A$  and  $L$  represent the free inside area and thickness of the Teflon ring.  $R_b$  is the bulk resistance obtained from the EIS measurements in the frequency range from 1 Hz to 4 MHz. The impedance measurements were carried out using a Zahner

**Table 1**

Composition, ionic conductivity and viscosity data of the investigated electrolytes.

Solvent	Conducting salt	$\sigma$ (mS cm <sup>-1</sup> ) (25 °C)	$\eta$ (mPa s) (25 °C)
EMIM-TFSA	LiPF <sub>6</sub> (0.5 M)	5.0 ± 0.4	54.4 ± 0.5
EMIM-TFSA/EC (7:3 v %)	LiPF <sub>6</sub> (0.5 M)	9.5 ± 0.8	19.2 ± 0.5
EMIM-TFSA/PC (7:3 v %)	LiPF <sub>6</sub> (0.5 M)	8.2 ± 0.6	23.4 ± 0.6
EC/DMC (1:1 v %)	LiPF <sub>6</sub> (1 M)	11.1 ± 1.0	3.6 ± 0.2

Zennium IM6 electrochemical workstation. The setup was calibrated with a 0.1 M KCl solution with a conductivity of 11.6 ± 1.0 mS cm<sup>-1</sup> (20 °C) [37]. The temperature dependence of the ionic conductivity was recorded by placing the test cells in a temperature and humidity chamber (Espec, SH-261). Before each measurement, the cells were equilibrated for at least 30 min. The dynamic viscosity of the electrolytes listed in Table 1 was measured using a Malvern Gemini HR Nano rotational rheometer. These experiments were performed in air. A measurement of the water uptake during and/or after the preparation and measuring of the viscosity was not possible. Therefore, we determined the uptake by using a glass vial (4.0 ml of solvent; diameter: 2 cm) which was in contact with air for 0–30 min. The water content increased by values of up to 50–150 ppm within 5–10 min in air (typical sample preparation time). After the preparation the solvent was protected by using a solvent/argon trap.

### 2.3. Cell assembly and electrochemical testing

Three different cell types were used in this study. For EIS measurements, two-electrode coin-type cells were assembled, while for SEM investigations three-electrode Swagelok-type cells were used. The *in situ* <sup>7</sup>Li nuclear magnetic resonance (NMR) experiments were performed on two-electrode pouch-bag type battery cells. All cells were assembled in an argon-filled glove box (O<sub>2</sub> < 1 ppm, MBraun GmbH, Germany) with lithium metal foil (Goodfellow, 99.9%, 200 µm thickness) as anode.

For both the impedance measurements and the SEM experiments, Li<sub>4</sub>Ti<sub>5</sub>O<sub>12</sub> thin film electrodes with a typical thickness of 25 µm were used. The active loading was typically 5.9 mg for EIS measurements and typically 3.6 mg for SEM. The diameter of the electrode disks was 14 mm for EIS and 12 mm for SEM. The cathode consists of a mixture of 80 wt% Li<sub>4</sub>Ti<sub>5</sub>O<sub>12</sub> (Südchemie AG, Germany), 10 wt% carbon black (Super P, Timcal) and 10 wt% polyvinylidene difluoride (PVDF, Arkema Inc.), dissolved in N-methyl-2-pyrrolidone (NMP, Sigma Aldrich). The slurry was cast onto a copper substrate (Goodfellow, 99.9%, 10 µm thickness). The electrode sheets were initially dried overnight at room temperature and then stored in an oven at 90 °C until further use. Coin-type cells with one sheet of Whatman GF/B (diameter 16 mm) were used for EIS measurements with the lithium metal electrode placed on a stainless steel plate.

For SEM investigations a Ni plate (diameter 12 mm) was used as anode current collector. Spatial separation between the electrodes was ensured by a small glass ring (thickness 4 mm, diameter 12 mm) with a thin Teflon ring (thickness 1.1 mm, diameter 12 mm) placed between the glass ring and the Li<sub>4</sub>Ti<sub>5</sub>O<sub>12</sub> electrode. Two stainless steel cylinders (diameter 12.7 mm) were aligned and pressed together with 4 N m controlled by a torque handle. Subsequently, the electrolyte solution was added through a small hole in the glass ring via the reference electrode opening.

For both the EIS measurements and SEM studies, the lithium/Li<sub>4</sub>Ti<sub>5</sub>O<sub>12</sub> battery cells were galvanostatically cycled between 1 V and 3 V with a constant current corresponding to a C/20 rate (i.e. complete discharge or charge within 20 h). The discharging and

<sup>1</sup> Alternative names in the literature include bis(trifluoromethanesulfonyl)imide (TFSI) and bis(trifluoromethanesulfonyl)amide (TFSA) [49].

charging process was performed at room temperature using a Biologic multi-channel potentiostat.

In order to prepare the test cells used for *in situ*  $^7\text{Li}$  NMR, a pouch bag design similar to Bellcore's setup [38–40] was adopted. The bag's foil (Lava Vakuumpackung) consists of polyethylene and polyamide. Both lithium/ $\text{Li}_4\text{Ti}_5\text{O}_{12}$  and symmetrical lithium/lithium test cells were assembled. The lithium electrode is built up from a lithium metal disk (diameter 5 mm) superimposed on a copper current collector mesh (100 mm  $\times$  5 mm  $\times$  0.05 mm, Dexmet). For the lithium titanate substrate, an aluminium mesh (100 mm  $\times$  5 mm  $\times$  0.05 mm, Dexmet) was used. The  $\text{Li}_4\text{Ti}_5\text{O}_{12}$  electrode was prepared by dip-coating the aluminium strip into the cathode slurry (8:1:1 weight ratio of  $\text{Li}_4\text{Ti}_5\text{O}_{12}$  powder, conductive carbon and PVDF binder dissolved in NMP). A porous glass micro-fiber filter disk (Whatman GF/B, 1 mm thickness) soaked with electrolyte solution served as separator. The cell components were assembled and the bag was sealed inside an argon-filled glove box. The test cells were cycled inside the superconducting NMR magnet using an Autolab potentiostat/galvanostat (Eco Chemie). The lithium/ $\text{Li}_4\text{Ti}_5\text{O}_{12}$  battery cells were subsequently discharged and charged in galvanostatic mode between 1 V and 3 V. Since the cathode preparation procedure provides no identical active masses of  $\text{Li}_4\text{Ti}_5\text{O}_{12}$ , the comparison of the investigated electrolytes might be handicapped by potential differences of the individual cells with respect to cycling time, cycle rate, and mass of  $\text{Li}_4\text{Ti}_5\text{O}_{12}$ , and applied current. In order to avoid this, symmetrical lithium/lithium cells were subject to a direct current of 50  $\mu\text{A}$  (current density of 0.26  $\text{mA cm}^{-2}$ ) for several hours.

#### 2.4. Electrochemical impedance spectroscopy

Electrochemical impedance measurements were carried out using a VMP3 multi-potentiostat from Biologic Science Instruments equipped with EIS option. The frequency range used was from 1 mHz to 500 kHz, starting from high frequency to low frequency in a logarithmic scan. The alternating voltage amplitude was set to 5 mV. In order to detect the influence of state-of-charge (SOC) on the impedance response, the cycling process was interrupted after 5, 10 and 15 h of Li insertion/removal and the impedance response was recorded at SOC values of 25%, 50% and 75%. For each new SOC, the battery cell was allowed to equilibrate for up to 2 h ( $|dE/dt| < 0.1 \text{ mV h}^{-1}$ ). Each EIS measurement was performed on at least two identical cells.

Modelling and simulation of the EIS data were performed using an equivalent circuit model. Quantitative analyses were done using Zview2 software (Scribner Associates, Inc.).

#### 2.5. Scanning electron microscopy

For imaging of the electrode in the scanning electron microscope, a method similar to that of Chen *et al.* [41] was used to prevent any exposure of the electrode surface to air/moisture before imaging. After cycling, the cells were disassembled in an argon-filled glove box and the electrodes were rinsed with diethyl carbonate (DEC) and dimethyl carbonate (DMC, 3  $\times$  2 ml) to remove any remaining salt from the surface of the electrodes. The lithium electrode was then adhered to a standard SEM stub using carbon tape which was inserted into a stainless steel transfer container. The container was closed inside the glove box and transferred to the SEM where it was pumped to approx. 10–5 mbar. After the SEM chamber reached the target vacuum level, the module was opened using the SEM stage rotation and the electrode surface was ready for inspection.

Imaging of the electrode surfaces was carried out in an FEI Nova Nanolab 200 at 10 kV. The electrical connection through the lithium

electrode appeared to be adequate as no charging was observed on the metal surface. Some residual organic contaminants were observed to charge on the surface of the electrode. In some cases, the residue even appeared to be volatile under irradiation from the electron beam. However, this residue was only found on certain regions and did not appear to cover the entire surface of the electrode.

#### 2.6. *In situ* $^7\text{Li}$ nuclear magnetic resonance spectroscopy

Static  $^7\text{Li}$  NMR was performed on a Bruker Avance 200 MHz spectrometer ( $B_0 = 4.7 \text{ T}$ ) at room temperature. A static probe with a flat solenoidal coil tuned at the  $^7\text{Li}$  frequency of 77.8 MHz was used for all experiments. The planes of the battery electrodes were oriented perpendicular to the magnetic field during all experiments. Series of spectra were recorded in uniform intervals of 1000 s during the entire electrochemical cycling.

$^7\text{Li}$ , due to its high natural abundance (93%), enables short measurement times. The values for the recycle delay of the symmetrical lithium/lithium and the lithium/ $\text{Li}_4\text{Ti}_5\text{O}_{12}$  cells are 1 s and 20 s, respectively. The delay values are chosen to minimize possible relaxation effects on the resulting spectra. The spectra of the symmetrical lithium/lithium and the lithium/ $\text{Li}_4\text{Ti}_5\text{O}_{12}$  cells were obtained through the acquisition of 2000 and 50 FID signals, respectively. The typical  $\pi/2$  pulse length is 5  $\mu\text{s}$ . An aqueous 1 M LiCl solution was used as the reference for the chemical shift of  $^7\text{Li}$  (0 ppm).

### 3. Results and discussion

#### 3.1. Electrolytes

Since the electrolyte conductivity plays a crucial role in understanding the electrochemical properties of the liquid electrolyte and the formation of lithium dendrites at the lithium metal surface, the temperature dependence of the conductivity was studied. Electrolyte compositions based on an ionic liquid, namely 1-ethyl-3-methylimidazolium bis(trifluoromethane-sulfonyl)azanide (EMIM-TFSA) were used. For comparison, a mixture of  $\text{LiPF}_6$  in EC/DMC was applied as well.

Fig. 1 depicts the conductivity of the studied electrolytes between 278 and 318 K. It should be noted that  $\text{LiPF}_6$  shows remarkable decomposition when the temperature exceeds 333 K. With increasing temperature, a rise in ionic conductivity can be observed. At 298 K, the conductivities of most of the electrolyte systems are comparable, with values in the range of 8–11  $\text{mS cm}^{-1}$ . However,  $\text{LiPF}_6$  in EMIM-TFSA exhibits an ion conductivity which is only half of the value of the remaining electrolytes. Furthermore, the temperature dependence of the ionic liquid mixtures is more pronounced than for the standard  $\text{LiPF}_6$  in EC/DMC system. Thus, the lithium transport in these solvents could be more sensitive to temperature changes.

#### 3.2. Electrochemical impedance spectroscopy

Fig. 2 depicts the voltage profile during the first discharging and charging process for a lithium/ $\text{Li}_4\text{Ti}_5\text{O}_{12}$  battery cell.  $\text{LiPF}_6$  in EMIM-TFSA/EC was used as electrolyte. Black circles mark states where EIS experiments were performed. The shape of the potential curve was found to be similar to those reported in the literature for standard electrolyte systems [32,42]. In addition to Yang *et al.* [43] extensive intercalation/extraction of lithium ions was performed and the frequency response was recorded at several state-of-charges. However, in the following, we focus on changes of the impedance

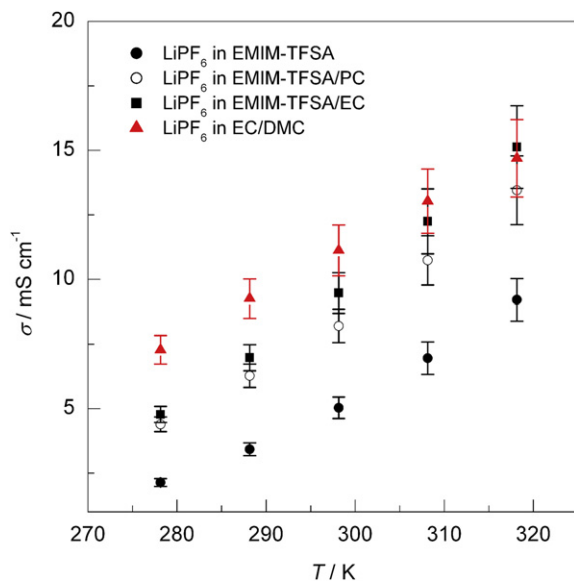


Fig. 1. Ionic conductivity of the electrolyte mixtures and its temperature dependence.

behaviour in subsequent cycles and analyse data obtained at the 50% state-of-charge during discharging.

Fig. 3 depicts the Nyquist diagrams of a lithium/ $\text{Li}_4\text{Ti}_5\text{O}_{12}$  cell at different cycle numbers. Here, the frequency response corresponds to 50% state-of-charge during discharging of the battery cell. The EIS data was quantitatively analyzed using the equivalent circuit model shown in Fig. 4. An excellent agreement between measurement and simulation data was obtained for all experiments.

While at high frequencies the inductive data (not shown in the figures) can be ascribed to the connection leads to the battery, the intercept with the x axis corresponds to the ohmic resistance of the battery cell, including the electrolyte resistance, contact resistances, electronic contacts, etc. [44–47]. These loss processes are implemented in the model by an inductance  $L$  and a resistance  $R_0$ ,

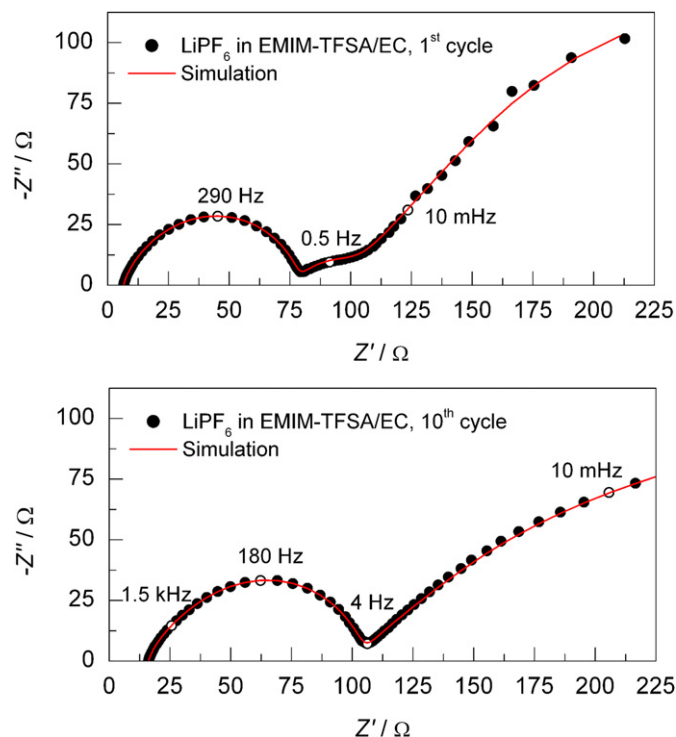


Fig. 3. Impedance spectra of a lithium/ $\text{Li}_4\text{Ti}_5\text{O}_{12}$  battery cell for different cycle numbers at 50% SOC during discharging.

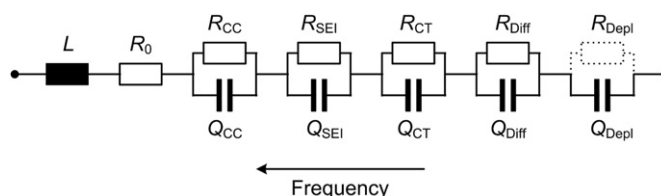


Fig. 4. Equivalent-circuit model of a coin-type lithium/ $\text{Li}_4\text{Ti}_5\text{O}_{12}$  cell [33].

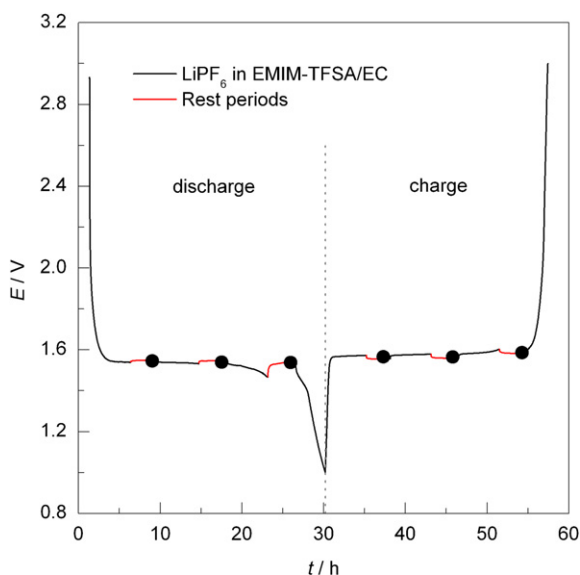


Fig. 2. Voltage profile during the first cycle for a lithium/ $\text{Li}_4\text{Ti}_5\text{O}_{12}$  coin-type battery cell.  $\text{LiPF}_6$  in EMIM-TFSA/EC was used as electrolyte solution. Black circles mark states where impedance measurements were performed.

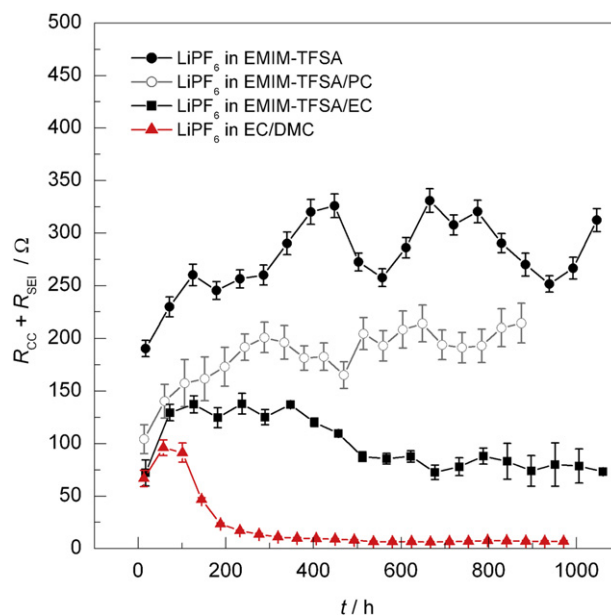


Fig. 5. Resistance values  $R_{CC} + R_{SEI}$  as a function of experimental time for several electrolyte solutions as given in the legend. The error bars just depict the errors from the fitting procedure.



respectively. Depressed semi-circles visible in the high-to-mid frequency range are expressed as an  $R$ – $Q$  element, i.e. a resistor in parallel with a constant-phase element. Here, the semi-circles are assigned to the current collector/ $\text{Li}_4\text{Ti}_5\text{O}_{12}$  interface ( $R_{\text{CC}}, Q_{\text{CC}}$ ) [34], the solid electrolyte interphase (SEI) layer at the Li metal surface ( $R_{\text{SEI}}, Q_{\text{SEI}}$ ) [34], and the charge transfer at the  $\text{Li}_4\text{Ti}_5\text{O}_{12}$ /electrolyte interface ( $R_{\text{CT}}, Q_{\text{CT}}$ ) [47]. At lower frequencies, solid-state diffusion as well as accumulation and depletion of lithium ions occur in the active material [44] and are represented by an additional  $R$ – $Q$  element in series with a constant phase element  $Q_{\text{Depl}}$  rather than Warburg diffusion. In order to describe the experimental data as a function of both state-of-charge and cycle number, an additional resistance  $R_{\text{Depl}}$  was included to allow for low-frequency data curving towards the x-axis.

In order to determine the influence of the different electrolyte solutions on the electrolyte/lithium interface, impedance measurements were performed. Here, in addition to Ref. [43], the impedance spectra were obtained during extensive cycling. Fig. 5 shows the resistance values  $R_{\text{CC}} + R_{\text{SEI}}$  as a function of time for different electrolyte systems, as indicated in the legend. A distinct split-up of the high-frequency arc into two separate semi-circles, as observed in Ref. [33], could not be seen for the electrolyte solutions based on the ionic liquid. However, the two different loss processes have been clearly resolved for the standard electrolyte system  $\text{LiPF}_6$  in EC/DMC. Thus, the sum of the resistances  $R_{\text{CC}}$  and  $R_{\text{SEI}}$  does not only describe the solid electrolyte interphase (SEI) layer at the lithium metal surface, but also includes the current collector/ $\text{Li}_4\text{Ti}_5\text{O}_{12}$  interface.

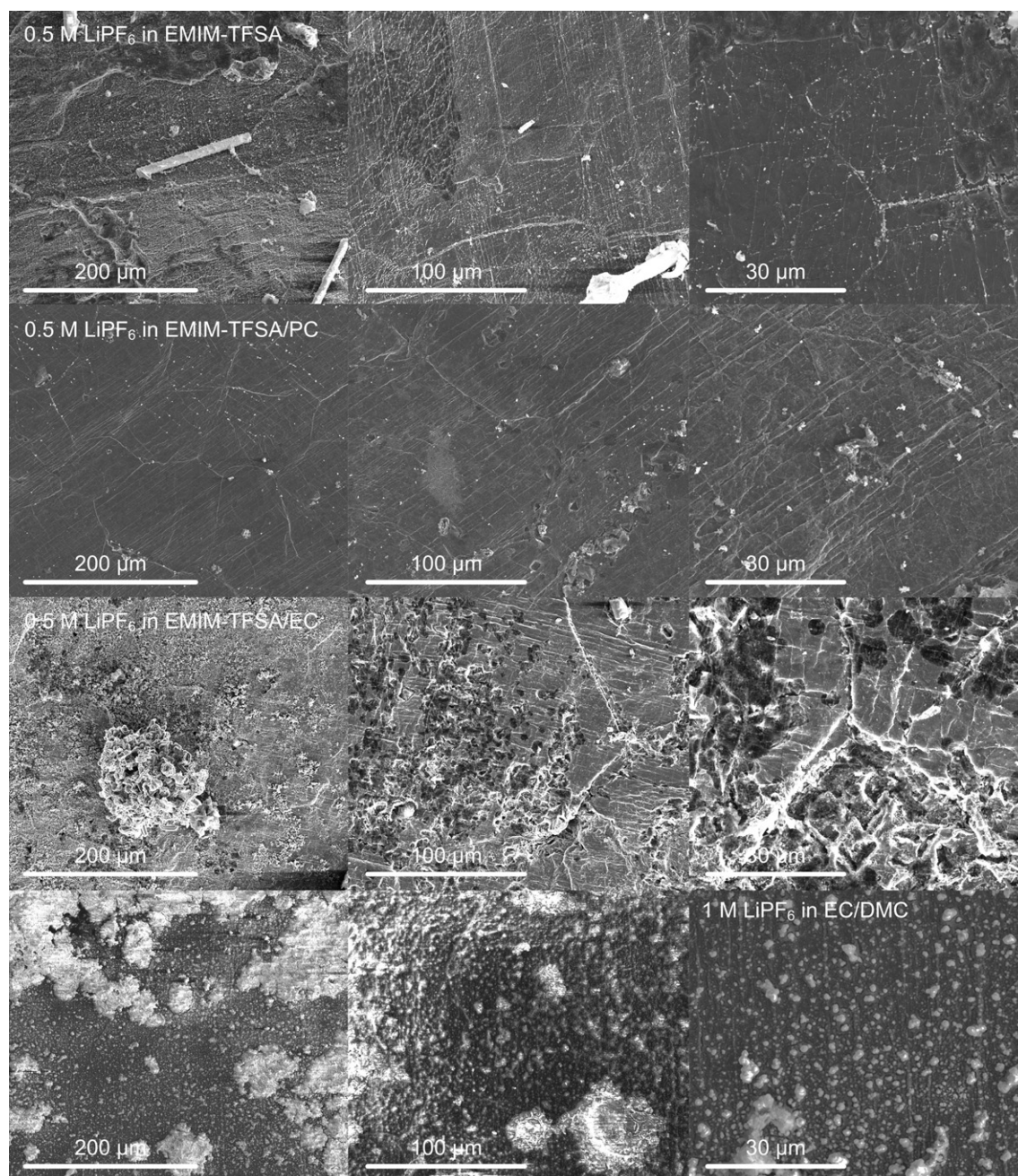


Fig. 6. SEM images of the lithium metal surface after 19 cycles in Swagelok-type lithium/ $\text{Li}_4\text{Ti}_5\text{O}_{12}$  cells.

Fig. 5 depicts a non-linear decrease of the resistance values  $R_{CC} + R_{SEI}$  with time for the standard electrolyte solution. According to our recent work, this drop is associated with an increase of the interfacial area between the electrolyte and the lithium metal electrode [34]. Thus, the formation of lithium dendrites or “mossy” structures at the anode surface can be observed in the impedance spectra of the lithium/ $\text{Li}_4\text{Ti}_5\text{O}_{12}$  battery cell. Based on this interpretation,  $\text{LiPF}_6$  in EMIM-TFSA/EC shows a moderate lithium dendrite formation. However, the curves of  $\text{LiPF}_6$  in EMIM-TFSA/PC and pure  $\text{LiPF}_6$  in EMIM-TFSA show no decrease in resistance but an overall increasing trend and, therefore, exhibit no dendrite formation at the interfacial region between electrolyte and lithium metal anode. Here, the scattering in the resistance values might be caused by temperature variations during the measurement, affecting the ionic conductivity and viscosity of the ionic liquids (cf. Fig. 1). In order to support this explanation, additional SEM investigations as well as *in situ*  $^7\text{Li}$  NMR experiments were performed.

### 3.3. Scanning electron microscopy

Fig. 6 depicts SEM images of the lithium surface after 19 cycles for different magnifications. The electrolyte solutions used in the test cells are indicated in the legend. The morphology of the metallic lithium surface appears to be significantly correlated to the electrolyte employed. The most noticeable changes at the lithium metal surface are observed when using  $\text{LiPF}_6$  in EC/DMC, whereas  $\text{LiPF}_6$  in EMIM-TFSA and  $\text{LiPF}_6$  in EMIM-TFSA/PC clearly suppress lithium dendrites most efficiently. The surfaces of these two samples show little to no evidence of extrusion or etching of the lithium metal.  $\text{LiPF}_6$  in EMIM-TFSA/EC shows moderate dendrite growth with clear signs of porosity in the surface of the electrode as material is removed to form dendrites. This rough lithium metal surface results in a high surface area and in a decrease of the resistance values as seen in Fig. 5. However,  $\text{LiPF}_6$  in EC/DMC exhibits an even rougher surface compared to the previous sample but the finer scale of surface features and residual organic contaminates on the surface make imaging difficult. The results of the SEM investigations are in agreement with the impedance measurements and support our findings.

### 3.4. *In situ* $^7\text{Li}$ nuclear magnetic resonance spectroscopy

NMR is a quantitative method, provided one can properly address the so-called “skin-depth problem” with lithium metal. The applied radio frequency field for excitation of the lithium nuclei penetrates only the surface region of metals [48]. Here, the experimental parameters lead to a penetration depth of  $14.7\ \mu\text{m}$ . Therefore, our measurements are sensitive to changes of the surface area in this range. Fig. 7 displays three  $^7\text{Li}$  NMR spectra of the lithium metal inside a lithium/ $\text{Li}_4\text{Ti}_5\text{O}_{12}$  cell containing the

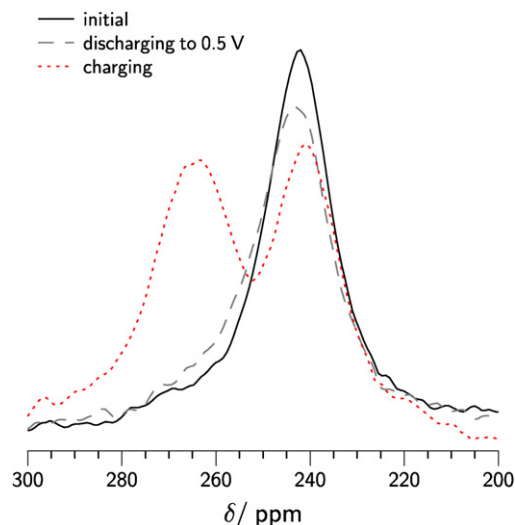


Fig. 7. *In situ*  $^7\text{Li}$  NMR spectra of a lithium/ $\text{Li}_4\text{Ti}_5\text{O}_{12}$  pouch cell containing  $\text{LiPF}_6$  in EC/DMC.

standard electrolyte  $\text{LiPF}_6$  in EC/DMC. The applied current was  $I = \pm 166\ \mu\text{A}$  (current density of  $0.59\ \text{mA cm}^{-2}$ ).

One of the spectra is obtained at the beginning of the first cycle, i.e. before discharging (full line), the second one is acquired at the end of the first discharge (dashed line), and the third one is recorded at the end of the first charge (short dashed line). While the first and the second spectrum show one resonance at approximately 242 ppm, two resonances, one at 242 ppm and one at 262 ppm, with similar intensities are observable in the third spectrum. In accordance with Bhattacharyya *et al.*, we interpret the occurrence of the two metal lithium resonances in terms of different surface structures on the lithium electrode [48]. During the discharging process, i.e. Li removal from the Li metal electrode, the lithium surface remains rather smooth, leading to a single resonance in the first spectrum. The right peak in the third spectrum, being at approximately the same position as the resonance in spectrum 1 and 2, can be assigned to the remains of the smooth lithium surface. The evolution of an additional resonance at 262 ppm can be readily explained by the deposition of lithium on the surface during charge, i.e. re-deposition of Li, resulting in the growth of mossy or dendritic structures.

Fig. 8 presents data obtained from lithium/lithium cells containing  $\text{LiPF}_6$  in EMIM-TFSA, in EMIM-TFSA/PC, in EMIM-TFSA/EC, and in EC/DMC, respectively (from left to right). Each diagram displays one spectrum measured at the beginning of the (dis-) charge, one measured after 5.5 h, and one measured after 11 h. Basically, all cells show characteristic spectral changes similar to the evolution in lithium/ $\text{Li}_4\text{Ti}_5\text{O}_{12}$  cells described above. Initially,

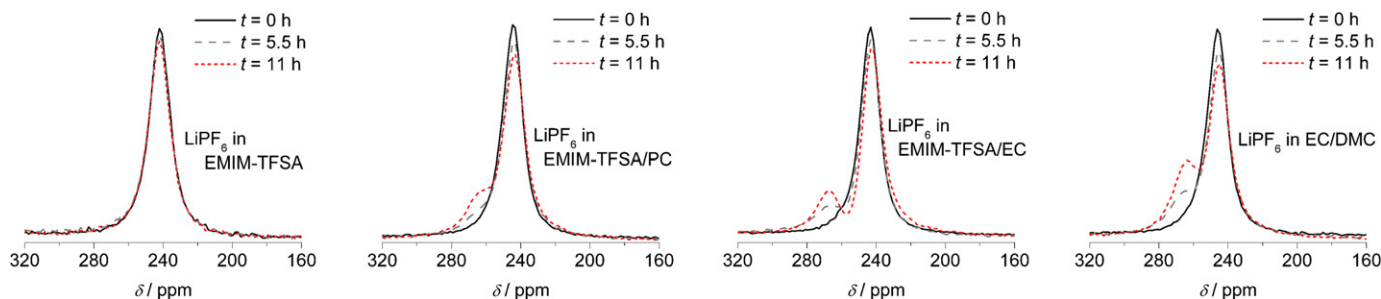


Fig. 8. *In situ*  $^7\text{Li}$  NMR spectra of symmetrical lithium/lithium pouch cells containing different electrolyte solutions.

only one resonance is observed and a second resonance increases with progress of time. The intensity of the second resonance is related to the electrolyte employed. Using  $\text{LiPF}_6$  in EC/DMC, the additional resonance is most pronounced, while for  $\text{LiPF}_6$  in EMIM-TFSA/EC and to an increasing degree for  $\text{LiPF}_6$  in EMIM-TFSA/PC the rise of this peak is significantly slowed down. The cell containing  $\text{LiPF}_6$  in EMIM-TFSA shows no second resonance during the standard observation time. Assigning the second peak's intensity to the quantity of dendritic structures on the lithium metal surface results in good accordance with the findings obtained via EIS and SEM.

#### 4. Conclusions

In this study, the formation of lithium dendrites at the lithium metal surface was studied using different experimental techniques. Electrochemical impedance spectroscopy and *in situ*  $^7\text{Li}$  nuclear magnetic resonance spectroscopy were used for non-invasive and quantitative analyses, whereas scanning electron microscopy was applied for visual inspection of dendrite growth and surface morphology. It is shown that all methods provide consistent and complementary results regarding lithium dendrite formation and evolution.

These investigations were performed on lithium/ $\text{Li}_4\text{Ti}_5\text{O}_{12}$  as well as symmetrical lithium/lithium test cells with different electrolyte solutions. Besides standard electrolyte solution, namely  $\text{LiPF}_6$  in EC/DMC, various electrolyte systems based on the ionic liquid EMIM-TFSA were used.

As a result, the formation of lithium dendrites or an increase of the surface area is significantly correlated to the electrolyte employed. The most noticeable changes at the lithium metal surface are observed using  $\text{LiPF}_6$  in EC/DMC.  $\text{LiPF}_6$  in EMIM-TFSA and  $\text{LiPF}_6$  in EMIM-TFSA/PC suppress lithium dendrites most efficiently. A moderate formation of dendritic structures and a rough lithium metal surface were observed for  $\text{LiPF}_6$  in EMIM-TFSA/EC.

#### Acknowledgements

We are grateful to the German Ministry for Education and Research for financial support. We thank Thomas Schubert and Maria Taige (IoLiTec GmbH, Heilbronn, Germany) for kindly providing the ionic liquids and Li Bing for fruitful discussions. S.T. Boles would like to thank the Alexander von Humboldt Foundation for their financial support.

#### References

- [1] K. Xu, Chem. Rev. 104 (2004) 4304.
- [2] J.-M. Tarascon, M. Armand, Nature 414 (2001) 359.
- [3] E.J. Cairns, P. Albertus, Annu. Rev. Chem. Biomol. Eng. 1 (2010) 299.
- [4] K.M. Abraham, Z. Jiang, J. Electrochem. Soc. 143 (1996) 1.
- [5] T. Ogasawara, A. Débart, M. Holzapfel, P. Novák, P.G. Bruce, J. Am. Chem. Soc. 128 (2006) 1390.
- [6] J.-S. Lee, S.T. Kim, R. Cao, N.-S. Choi, M. Liu, K.T. Lee, J. Cho, Adv. Energy Mater. 1 (2011) 34.
- [7] J. Shim, K.A. Striebel, E.J. Cairns, J. Electrochem. Soc. 149 (1999) A1321.
- [8] R.D. Rauh, K.M. Abraham, G.F. Pearson, J.K. Surprenant, S.B. Brummer, J. Electrochem. Soc. 126 (1979) 523.
- [9] X. Li, K.T. Lee, L.F. Nazar, Nat. Mater. 8 (2009) 500.
- [10] E. Peled, J. Electrochem. Soc. 126 (1979) 2047.
- [11] M. Winter, J.O. Besenhard, Chem. Unserer Zeit 33 (1999) 320.
- [12] S.W. Kim, Y.J. Ahn, W.Y. Yoon, Met. Mater.-Korea 6 (2000) 345.
- [13] J.L. Tirado, Mater. Sci. Eng. R40 (2003) 103.
- [14] J. Yamaki, S. Tobishima, K. Hayashi, K. Saito, Y. Nemoto, M. Arakawa, J. Power Sources 74 (1998) 219.
- [15] I. Yoshimatsu, T. Hirai, J. Yamaki, J. Electrochem. Soc. 135 (1988) 2422.
- [16] K. Nishikawa, T. Mori, T. Nishida, Y. Fukunaka, M. Rosso, T. Homma, J. Electrochem. Soc. 157 (2010) A1212.
- [17] F. Orsini, A. Du Pasquier, B. Beaudoin, J.-M. Tarascon, M. Trentin, N. Langenhuisen, E. De Beer, P. Notten, J. Power Sources 76 (1998) 19.
- [18] F. Orsini, A. Du Pasquier, B. Beaudoin, J.-M. Tarascon, M. Trentin, N. Langenhuisen, E. De Beer, P. Notten, J. Power Sources 81 (1999) 918.
- [19] M. Dollé, L. Sannier, B. Beaudoin, M. Trentin, J.-M. Tarascon, Electrochem. Solid-State Lett. 5 (2002) A286.
- [20] D. Aurbach, I. Weissman, H. Yamin, E. Elster, J. Electrochem. Soc. 145 (1998) 1421.
- [21] A. Lewandowski, A. Swiderska-Mocek, J. Appl. Electrochem. 40 (2010) 515.
- [22] D. Aurbach, B. Markovsky, A. Schechter, Y. Ein-Eli, H. Cohen, J. Electrochem. Soc. 143 (1996) 3809.
- [23] D. Aurbach, A. Zaban, A. Schechter, Y. Ein-Eli, E. Zinigrad, B. Markovsky, J. Electrochem. Soc. 142 (1995) 2873.
- [24] T. Hirai, I. Yoshimatsu, J. Yamaki, J. Electrochem. Soc. 141 (1994) 611.
- [25] T. Hirai, I. Yoshimatsu, J. Yamaki, J. Electrochem. Soc. 141 (1994) 2300.
- [26] I.W. Seong, C.H. Hong, B.K. Kim, W.Y. Yoon, J. Power Sources 178 (2008) 769.
- [27] J.S. Kim, W.Y. Yoon, K.Y. Yi, B.K. Kim, B.W. Cho, J. Power Sources 165 (2007) 620.
- [28] C. Brissot, M. Ross, J.-N. Chazalviel, S. Lascaud, J. Power Sources 81–82 (1999) 925.
- [29] T. Sato, T. Maruo, S. Marokane, K. Takagi, J. Power Sources 138 (2004) 253.
- [30] G.B. Appetecchi, G.-T. Kim, M. Montanino, M. Carewska, R. Marcella, D. Mecerreyes, I. De Meazza, J. Power Sources 195 (2010) 3668.
- [31] J.R. Macdonald, Ann. Biomed. Eng. 20 (1992) 289.
- [32] T. Ohzuku, J. Electrochem. Soc. 142 (1995) 1431.
- [33] J. Ma, C. Wang, S. Wroblewski, J. Power Sources 164 (2007) 849.
- [34] N. Schweikert, H. Hahn, S. Indris, Phys. Chem. Chem. Phys. 13 (2011) 6234.
- [35] N. Schweikert, R. Heinzmann, A. Eichhöfer, H. Hahn, S. Indris, Solid State Ionics 226 (2012) 15.
- [36] N.M. Trease, L. Zhou, H.J. Chang, B.Y. Zhu, C.P. Grey, Solid State Nucl. Magn. Reson. 42 (2011) 62.
- [37] S.D. Hamann, M. Linton, Trans. Faraday Soc. 65 (1969) 2196.
- [38] J.-M. Tarascon, A.S. Gozdz, C. Schmutz, F. Shokoohi, P.C. Warren, Solid State Ionics 86–88 (1996) 49.
- [39] F. Chevallier, M. Letellier, M. Morcrette, J.-M. Tarascon, E. Frackowiak, J.-N. Rouzaud, F. Béguin, Electrochem. Solid-State Lett. 6 (2003) A225.
- [40] M. Letellier, F. Chevallier, C. Clinard, E. Frackowiak, J.-N. Rouzaud, F. Béguin, J. Chem. Phys. 118 (2003) 6038.
- [41] D. Chen, S. Indris, M. Schulz, B. Garner, R. Mönig, J. Power Sources 196 (2011) 6382.
- [42] G.X. Wang, D.H. Bradhurst, S.X. Dou, H.K. Lui, J. Power Sources 83 (1999) 156.
- [43] L. Yang, C. Smith, C. Patrissi, C.R. Schumacher, B.L. Lucht, J. Power Sources 185 (2008) 1359.
- [44] C. Chen, J. Lui, K. Armine, J. Power Sources 96 (2001) 321.
- [45] B. Boukamp, Solid State Ionics 62 (1993) 131.
- [46] M. Gaberscek, J. Moskon, E. Erjavec, R. Dominko, J. Jamnik, Electrochem. Solid-State Lett. 11 (2008) A170.
- [47] H. Kaitera, A. Hayashi, K. Tadanaga, M. Tutsumisago, J. Electrochem. Soc. 156 (2009) A114.
- [48] R. Bhattacharyya, B. Key, H. Chen, A.S. Best, A.F. Hollenkamp, C.P. Grey, Nat. Mater. 9 (2010) 504.
- [49] G.J. Wilson, A.F. Hollenkamp, A.G. Pandolfo, Chem. Int. 29 (2007) 16.